

SUBMISSION TO COMBUSTION THEORY AND MODELLING

Reduction of a Detailed Soot Model for Simulations of Pyrolyzing Solid Fuels

Alexander J. Josephson^{a,b}, Emily M. Hopkins^{a,c}, David O. Lignell^b, and Rod R. Linn^a

^aEarth and Environmental Sciences Division, Los Alamos National Laboratory, Los Alamos, New Mexico, United States.

^bDepartment of Chemical Engineering, Brigham Young University, Provo, Utah, United States.

^cDepartment of Chemical Engineering, University of New Mexico, Albuquerque, New Mexico, United States.

ARTICLE HISTORY

Compiled August 9, 2019

ABSTRACT

This work presents a computationally inexpensive soot formation model for use in simulating large solid-complex fuel systems. The proposed model evaluates three variables: number density of tars, bulk mass density of soot particles, and particle number density. Each of these variables are influenced by soot formation phenomena, and this model evaluates the most common of these phenomena: soot nucleation, surface reactions, and coagulation. Two separate simulations were carried out using this model and results were compared against simulations using a more detailed and computationally expensive model. Results are promising and show a meaningful reduction in model complexity and computational cost while still giving comparable results.

KEYWORDS

soot; coal; biomass

1. Introduction

Predicting the formation of soot in combustion systems has been a research challenge for decades [1]. While the phenomena of soot formation has been well-studied in gaseous fuel systems and sophisticated models have been developed [2–9], the processes are less studied in solid fuel systems and there are few models available for predicting soot yields [10, 11].

The first step in the formation of soot particles is the nucleation of an incipient particle from soot precursors [12]. Differences in soot formation from gaseous and solid fuels is rooted in the source of system precursors. For gaseous fuels, soot precursors are polycyclic aromatic hydrocarbons (PAHs). These PAHs form from the gas-phase through a variety of chemical mechanisms [5, 13]. The formation of PAHs in fuel-rich regions of a flame often acts as a rate-limiting step to the soot formation process, putting constraints on both soot mass yield and particle size.

For solid fuels, soot precursors are primarily tars released from the parent fuel during primary pyrolysis [14, 15]. Unlike PAHs, which are organic aromatics, tars from solid fuels contain mixtures of aromatics/aliphatics and organics/heteroatoms. These differences in the

precursors may perpetuate in the reactivity of soot particles themselves [16, 17]. More importantly, pyrolysis of the parent fuel tends to release a much larger concentration of tars than any concentration of PAH build-up that we see in gaseous-fuel systems, indicating a much higher potential for soot formation in solid-fuel systems [14, 18].

Unfortunately, tars released from pyrolysis represent hundreds of possible species [18] all reacting in different ways. This pseudo-species, tar, is difficult to model. When we add to this some of the inherent complexities of modeling soot (complex chemical kinetics, changing particle morphology, and representing particle-size distributions), developing and computing a detailed, physics-based soot mechanism for solid fuels quickly becomes both difficult and computationally expensive.

Previously, a model was developed which captured many of these complexities [19]. Unfortunately, the previous model was computationally too expensive for use in large-scale simulations. This work purposes a reduced model for use in large-scale systems predicting the formation of soot from solid fuels.

2. Model Development

The proposed model solves rates for three quantities: the number density of tar molecules (N_{tar}), the number density of soot particles (N_{soot}), and the bulk mass density of soot particles (M_{soot}). Transport equations for these quantities may be written for use in various simulation approaches, but the generation/consumption rates for each term are defined here by submodels common to soot formation:

$$\frac{dN_{tar}}{dt} = r_{TI} - 2r_{SN} - r_{TD} - r_{TC} + 2508N_{tar}r_{TS}, \quad (1)$$

$$\frac{dM_{soot}}{dt} = 2m_{tar}r_{SN} + m_{tar}r_{TD} + \pi d_{soot}^2 N_{soot} r_{SS}. \quad (2)$$

$$\frac{dN_{soot}}{dt} = r_{SN} - r_{SC}, \quad (3)$$

These equations include terms for tar inception (r_{TI}), tar deposition (r_{TD}), thermal cracking (r_{TC}), soot nucleation (r_{SN}), soot coagulation (r_{SC}), and surface reactions (r_{TS} and r_{SS}). These terms are described in the following sections. The primary reduction of the soot formation model presented in this paper deals with the representation of tar and soot as mono-dispersed particle size distributions with the molecular weight of tars computed at inception then held constant and the particle weight of soot particles modeled along with number densities for both tar molecules and soot particles. As the molecular weight of tar is fixed, the transport of the tar number density accounts for the tar mass balance.

The reduction of complex models to simple particle number and bulk mass densities to represent a soot distribution is not original to this work [10, 20–22], and equations for many of these terms (soot nucleation, soot coagulation, and soot surface reactions) may be found in various forms throughout the literature. However, the coupling of these equations to a tar source term and the simplification of that species in the following sections represents the bulk of the novelty in this work.

2.1. Tar Inception

In a solid-fuel system, the formation of precursors is a summation of two sources: PAH build-up from light gases and the release of tar volatiles during primary pyrolysis. The proposed model dismisses the PAH build-up from light gases as a negligible source of precursors [14]; however, should researchers determine that a particular system for which this model is applied contains a significant build-up of PAH, inclusion of a PAH mechanism should be straightforward.

Precursor inception from the release of tar volatiles is modeled using a ‘sooting potential’ model unique to fuel type and pyrolysis conditions. This model is a calibrated surrogate model that predicts the mass fraction of volatiles (resulting from primary pyrolysis) which are tar (y_{tar}) along with their average molecular size (m_{tar}). Using the sooting potential model, either for biomass or for coal, we may predict the rate of tar inception as a fraction of the rate volatiles are released during primary pyrolysis r_v (kg/m³s),

$$r_{TI} = \frac{y_{tar}\dot{r}_v}{m_{tar}}, \quad (4)$$

for which there are many developed models [23–26].

2.1.1. Biomass

To develop the sooting potential model, the coal percolation model for devolatilization (CPD) [26] along with its biomass adaptation (CPDbio) [27] were used as standards for calibration. CPD is a network devolatilization model designed to predict products of primary pyrolysis for solid fuels. CPD-CP, a specific CPD iteration [28], contains a submodel combination for predicting particle temperature profiles if a user specifies the surrounding gas temperatures, pressure, and particle velocities; this particle temperature profile, along with CNMR (¹³C nuclear magnetic resonance) parameters of a fuel, are fed into the CPD portion of the code to predict pyrolysis behavior. To calibrate the sooting potential model, CPD-CP was executed thousands of times varying input parameters to create a comprehensive data set to which parameters could be tuned. During the calibration of the sooting potential model, it was quickly found that fuel particle velocities had a minimal effect on total tar yield and tar size and so particle velocities were kept constant 2.5E-5 (m/s) for the data creation.

CPDbio-CP was used to calibrate the sooting potential model for biomass fuels. When using CPDbio, predicting products of biomass primary pyrolysis is accomplished by first predicting the devolatilization behavior of five biomass components: cellulose, galacto-glucmannose (softwood hemicellulose), xylose (hardwood hemicellulose), softwood lignin (with higher concentrations of guaiacyl constituents), and hardwood lignin (with higher concentrations of syringyl constituents). Each component is determined independently and summed together, weighted by the respective mass percentage of each component in a given biomass, to predict the overall devolatilization behavior of the given biomass species.

CPDbio was executed 1000 times for each biomass component over a wide range of pressures and gas temperatures, 0.1 < P (atm) < 100 and 800 < T (K) < 3000, using a Latin hypercube sampling method. This generated 1000 data points to which rational empirical models of the forms

$$y_{tar} = \frac{a + bT_g + cP_l + dT_g^2 + eP_l^2 + fT_gP_l + gT_g^3 + hT_g^2P_l + iT_gP_l^2 + jP_l^3}{k + lT_g + mP_l + nT_g^2 + oP_l^2 + pT_gP_l + qT_g^3 + rT_g^2P_l + sT_gP_l^2 + tP_l^3}, \quad (5)$$

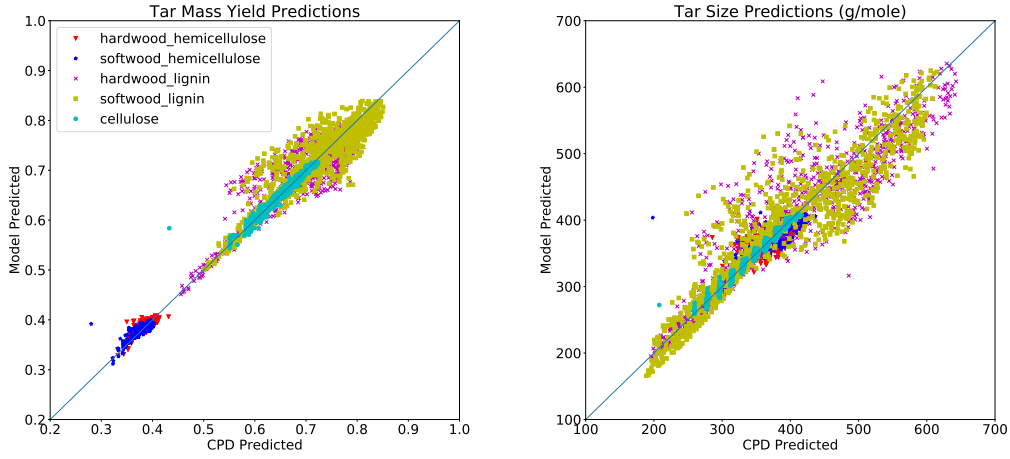


Figure 1.: Comparison between results given by CPDbio versus the proposed sooting potential empirical model. Different colors represent different biomass components: cellulose (blue), hemicellulose softwood/hardwood (green/yellow), and lignin softwood/hardwood (magenta/red). The left plot shows the comparison for tar mass yield ($R^2=0.811$) and the right plot shows the comparison for tar mass size ($R^2=0.856$).

$$m_{tar} = \frac{a + bT_g + cP_l + dT_g^2 + eP_l^2 + fT_gP_l + gT_g^3 + hT_g^2P_l + iT_gP_l^2 + jP_l^3}{k + lT_g + mP_l + nT_g^2 + oP_l^2 + pT_gP_l + qT_g^3 + rT_g^2P_l + sT_gP_l^2 + tP_l^3}, \quad (6)$$

were fitted. y_{tar} is the mass fraction of volatiles which is tar and m_{tar} is the average molecular mass of those tar species. In Equations 5 and 6, T_g represents the gas temperature (K) and P_l represents the logarithm (base 10) of the pressure (atm). Calibration was accomplished using a series of least-squares fittings for all 20 parameters. Insignificant parameters (those with an influence less than 2% on final yields and sizes) were eliminated and the proposed models refitted leaving the equations shown in Table 1. Like CPDbio, the sooting potential model predicts behavior for five different biomass components. To find the total biomass devolatilization behavior, simply sum together those components weighted by the mass fraction of the given component in the biomass

$$y_{tar} = y_{tar,cell}y_{cell} + y_{tar,hw/hc}y_{hw/hc} + y_{tar,sw/hc}y_{sw/hc} + y_{tar,hw/lig}y_{hw/lig} + y_{tar,sw/lig}y_{sw/lig}, \quad (7)$$

$$m_{tar} = m_{tar,cell}y_{cell} + m_{tar,hw/hc}y_{hw/hc} + m_{tar,sw/hc}y_{sw/hc} + m_{tar,hw/lig}y_{hw/lig} + m_{tar,sw/lig}y_{sw/lig}. \quad (8)$$

Note that this sooting potential model neglects the behavior of extractives (the final and smallest component of biomass) in part because extractives can vary so greatly that an individual characterization would need to be done for every species, which is not possible in a general model such as this. Fortunately, extractives typically make up a small mass fraction of most biomass species (approximately 1-5%) [29].

Figure 1 shows the effectiveness of this empirical sooting potential model against CPDbio. Both of these plots are parity plots where results of the sooting potential model are plotted against the x-axis while results of CPDbio are plotted against the y-axis. The black 45° line

Table 1.: Sooting potential model for biomass with calibrated parameters in Equations 5 and 6. T_g and P_l are the gas temperature (K) and logarithm (base 10) of the pressure (atm), respectively.

Component	Model
Cellulose	$y_{tar,cell} = \frac{-1.57E5+290.6T_g-0.022T_g^2+8.00T_gP_l+3.60E-5T_g^3-0.036T_g^2P_l}{-2.03E5+382.9T_g+11.2T_gP_l+4.53E-5T_g^3-0.042T_g^2P_l}$ $m_{tar,cell} = \frac{-3.06E4+242.2T_g+1.05E4P_l-1.84E3P_l^2-83.1T_gP_l+461.8P_l^3}{0.635T_g-0.145T_gP_l-0.021T_gP_l^2-2.78P_l^3}$
Hardwood Hemicellulose	$y_{tar,hw/hc} = \frac{-5.21E5+3.12E3T_g-0.382T_g^2-1.08E3T_gP_l+0.207T_g^2P_l}{5.75E3T_g-2.65E3T_gP_l-1.45E-4T_g^3+0.518T_g^2P_l}$ $m_{tar,hw/hc} = \frac{236.7T_gP_l^2-5.92E4P_l^3}{0.608T_gP_l^2-109.4P_l^3}$
Softwood Hemicellulose	$y_{tar,sw/hc} = \frac{7.05E4+144.4T_g-1.29E-5P_l+0.233T_g^2-7.41E-5T_g^3}{3.69E5+91.0T_g-3.22E5P_l+0.725T_g^2-2.08E-4T_g^3}$ $m_{tar,sw/hc} = \frac{-6.41E4P_l^2+50.0T_gP_l+26.0T_gP_l^2+1.56E4P_l^3}{-1.65E3P_l^2+0.126T_gP_l+0.072T_gP_l^2+41.3P_l^3}$
Hardwood Lignin	$y_{tar,hw/lig} = \frac{9.04E4-76.2T_g-3.43E4P_l+6.03E-3T_g^2+36.6T_gP_l+7.69E-6T_g^3-0.011T_g^2P_l}{1.37E5-117.5T_g-3.66E4P_l+0.012T_g^2+39.3T_gP_l+1.00E-5T_g^3-0.012T_g^2P_l}$ $m_{tar,hw/lig} = \frac{4.78E6-8.40E3T_g+7.36T_g^2+3.39E6P_l^2-573.1T_gP_l-1.23E-3T_g^3+340.1T_gP_l^2-4.85E5P_l^3}{8.13T_g+1.47E4P_l^2-2.64T_gP_l^2+997.9P_l^3}$
Softwood Lignin	$y_{tar,sw/lig} = \frac{470.5-0.303T_g-165.4P_l+3.22E-5T_g^2+0.124T_gP_l+6.46E-9T_g^3-2.37E-5T_g^2P_l}{735.3-0.550T_g-176.0P_l+1.05E-4T_g^2+0.133T_gP_l-2.56E-5T_g^2P_l}$ $m_{tar,sw/lig} = \frac{115.8P_l-29.7P_l^2+0.117T_gP_l-3.86E-5T_g^2P_l+3.46E-3T_gP_l^2-2.16P_l^3}{0.887P_l+0.118P_l^2-2.19E-4T_gP_l-4.00E-5T_gP_l^2-0.012P_l^2}$

represents a perfect match between the two models. As can be seen in the figures, the sooting potential model follows the trends of CPDbio with good agreement ($R^2=0.811$ and 0.856 for soot mass yield and molecular size respectively) but there is room for improvement should a better model form be found that is as computationally inexpensive as this proposed one.

2.1.2. Coal

To create a sooting potential model for coal fuels we needed to explore additional variables reflecting ^{13}C NMR parameters. These parameters may be obtained through a correlation developed by Genetti et al. [28] which links these parameters to the elemental composition and volatile matter content of the parent coal. Through this correlation and the use of CPD-CP, we again developed a database of 1000 data points varying O/C atomic ratio ($0.01 < O_C < 0.35$), H/C atomic ratio ($0.3 < H_C < 1.1$), volatile matter content ($2 < \text{Vol} (\%) < 80$), pressure ($0.1 < P (\text{atm}) < 100$), and gas temperature ($800 < T (\text{K}) < 3000$). This database was used in a similar way to calibrate surrogate models of a form similar to Equations 5 and 6; as before, negligible parameters were eliminated leaving

$$y_{tar} = \frac{-124.2 + 35.7P_l + 93.5O_C - 223.9O_C^2 + 284.8H_C - 107.3H_C^2 + 5.48V + 0.014V^2 - 58.2P_lH_C - 0.521P_lV - 5.32H_CV}{-303.8 + 52.4P_l + 1.55E3O_C - 2.46E3O_C^2 + 656.9H_C - 266.3H_C^2 + 15.9V + 0.025V^2 - 90.0P_lH_C - 462.5O_CH_C + 4.80O_CV - 17.8H_CV} \quad (9)$$

and

$$m_{tar} = \frac{3.12E5 + 16.4T_g + 4.34E5O_C - 8.48E5H_C + 6.38E5H_C^2 - 361.3V - 0.221T_gV - 6.39E5O_CH_C + 1.91E3H_CV}{753.6 + 0.042T_g + 83.9O_C - 1.77E3H_C + 1.20E3H_C^2 + 5.09E-3T_gP_l - 0.024T_gH_C - 5.27E-4T_gV + 0.513P_lV - 361.0O_CH_C + 3.83H_CV} \quad (10)$$

In these equations P_l is the logarithm of the pressure (atm). O_C and H_C are the atomic ratios of oxygen-carbon and hydrogen-carbon, respectively. V is the mass percent of volatile matter in the parent coal. T_g is the gas temperature. Unlike biomass, these surrogate models are absolute for predicting the tar mass yield and average molecular weight as a result of pyrolysis and do not need to be recombined from components.

Figure 2 shows the effectiveness of this empirical sooting potential model against CPD. Generally the sooting potential model follows the trends of CPD with good agreement ($R^2=0.794$ and 0.854 for soot mass yield and molecular size, respectively). It is interesting to note that in calibrating these surrogate models all gas temperature terms dropped out of Equation 9 as negligible and pressure only has a minor role in determining tar size (Equation 10). These characteristics show potential for further investigation in creating a more physics-based sooting potential model.

The largest advantage of using the developed sooting potential model is being able to retain the accuracy of the CPD model with computational cost-efficiency. To give a rough idea of the economy of these surrogates, running a Fortran implementation of CPD on a single processor took 2392 seconds to obtain the x-axis of the data shown in Figure 1. In contrast, running a Python implementation of these surrogate models combined with a fitted first-order weighted yield model (FOWY) for devolatilization, the y-axis data of the same figure, was obtained in 0.3 seconds. While this comparison is not perfect, it should convey that the surrogate models are more computationally efficient for large-scale simulations.

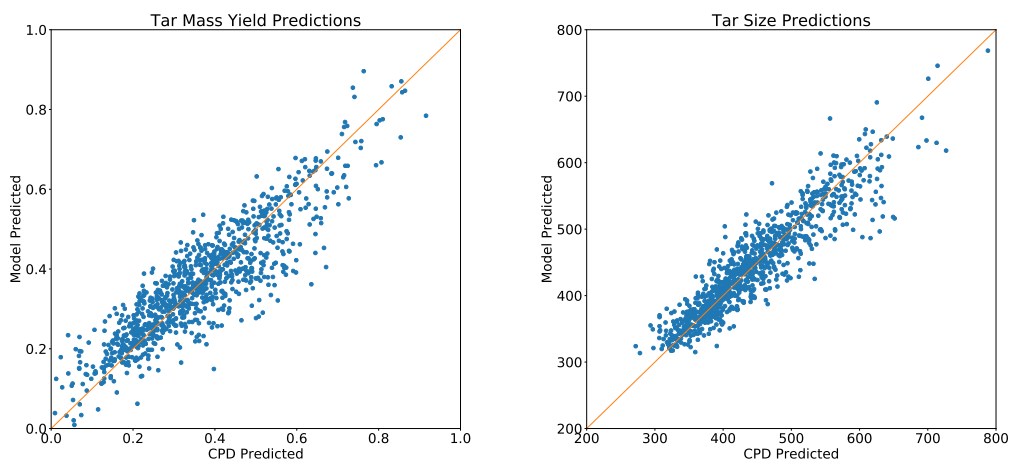


Figure 2.: Comparison between results given by CPD versus the proposed sooting potential empirical model. The left plot shows the comparison for tar mass yield ($R^2=0.794$) and the right plot shows the comparison for tar mass size ($R^2=0.854$).

2.2. Thermal Cracking

Thermal cracking is the chemical break-up of larger molecules, such as tars, into lighter gases and is heavily influenced both by the chemistry of the molecule and temperature [30, 31]. Tar volatiles, the soot precursors of this model, are not completely made up of aromatic rings but rather contain aliphatic and non-carbon components, reflective of the parent fuel [32]. These heteroatoms and aliphatic groups make tars more receptive to thermal cracking [33].

Thermal cracking of the tar is represented using a model developed by Marias et al. [34]. In this model, tars are characterized as four basic types: phenol, toluene, naphthalene, and benzene. While tars are not actually phenol, toluene, naphthalene, or benzene, these four species are used as surrogates. In mathematical terms we may say 1 mole of tar is taken as 1 mole of a mixture of phenol, toluene, naphthalene, and benzene. Each of these types undergo different reactions. These reactions either convert one type to another with the difference of mass being released into the gas phase, or crack completely into lighter gases. The rates of each of these reactions are given in Table 2.

The Marias model is translated into a number density change of tar by multiplying the rates of reaction by the fraction of molecular weight cracked into light gas,

$$r_{TC} = \left(\frac{31.1}{94} k_1 x_{phe} + k_2 x_{phe} + \frac{50}{128} k_3 x_{naph} [H_2]^{0.4} + \frac{14}{92} k_4 x_{tol} [H_2]^{0.5} + k_5 x_{ben} \right) N_i^{tar}, \quad (11)$$

where k_n values are given in Table 2. Square brackets denote species concentration in $\frac{\text{kmole}}{\text{m}^3}$. x_{phe} , x_{naph} , x_{tol} , and x_{ben} are the mole fractions of surrogate tars. The difficulty in using this submodel lies in specifying the x_{phe} , x_{naph} , x_{tol} , and x_{ben} values. In this study a surrogate model is created which may be used to determine the values of these parameters.

To form this surrogate model, a numerical study was conducted to observe the evolution of tar molecules in various combustion scenarios. This numerical study was performed by evolving an initialized group of tars using the cracking scheme detailed in Table 2 and the soot nucleation scheme detailed later in Section 2.3 until 95% of the tars are fully converted to light

Table 2.: Reactions and reaction rates used in tar cracking scheme (rates in $\frac{kmole}{m^3s}$, concentrations in $\frac{kmole}{m^3}$, and activation energies in $\frac{J}{mole K}$).

Reaction	Rates
$C_6H_6O \longrightarrow CO + 0.4C_{10}H_8 + 0.15C_6H_6 + 0.1CH_4 + 0.75H_2$	$R_1 = k_1[C_6H_6O]$ $k_1 = 1.00E7 \exp\left(\frac{-1.0E5}{RT}\right)$
$C_6H_6O + 3H_2O \longrightarrow 2CO + CO_2 + 3CH_4$	$R_2 = k_2[C_6H_6O]$ $k_2 = 1.00E8 \exp\left(\frac{-1.0E5}{RT}\right)$
$C_{10}H_8 + 4H_2O \longrightarrow C_6H_6 + 4CO + 5H_2$	$R_3 = k_3[C_{10}H_8][H_2]^{0.4}$ $k_3 = 1.58E12 \exp\left(\frac{-3.24E5}{RT}\right)$
$C_7H_8 + H_2 \longrightarrow C_6H_6 + CH_4$	$R_4 = k_4[C_7H_8][H_2]^{0.5}$ $k_4 = 1.04E12 \exp\left(\frac{-2.47E5}{RT}\right)$
$C_6H_6 + 5H_2O \longrightarrow 5CO + 6H_2 + CH_4$	$R_5 = k_5[C_6H_6]$ $k_5 = 4.40E8 \exp\left(\frac{-2.2E5}{RT}\right)$

gases or soot particles. The initial concentrations of the various tar types were determined by fuel oxygen mass fraction and the aromatic/aliphatic carbon ratio. The time averaged mole fractions of the tars were computed and used as data to calibrate the surrogate model. This numerical study was executed over a wide range of inputs, temperature, oxygen mass fraction, aromatic/aliphatic carbon ratio, H₂ concentration, and total initial tar number density, to generate data. This series of studies revealed that the two most important parameters for determining type fractions were temperature and initial tar number density. The other three parameters, oxygen mass fraction, aromatic/aliphatic carbon ratio, and H₂ concentration, all had negligible effects on the time-averaged tar type ratios.

Figure 3 shows the results of varying temperature (left) and initial number density (right) over a wide range, $500 < T \text{ (K)} < 3000$ and $1E10 < N_{tar} \text{ (\#/m}^3\text{)} < 1E25$. Observe that at low temperatures and high number densities the fractions all collapse to 1/3, corresponding to the initialization of the numerical study. This collapse is because at these conditions thermal cracking, which is temperature dominated, becomes negligible in comparison to soot nucleation mechanisms, which are concentration dependent. On the other hand, at high temperatures the thermal cracking dominates soot nucleation, and as a result phenol and toluene-type tars disappear quickly, being converted to a benzene-type. It is evident with the varying temperature plot that in terms of reactivity, phenol > toluene > naphthalene/benzene, which is expected because of the presence of oxygen in phenol, and aromatics are molecularly more stable than aliphatics.

Using the results of Figure 3, an empirical model was proposed of a form which captures the ‘S’ shape of the response surface (tanh),

$$x_i = \frac{\tanh(a + bT + cC_l + dT^2 + eC_l^2 + fTC_l)}{m} + g + hT + iC_l + jT^2 + kC_l^2 + lTC_l, \quad (12)$$

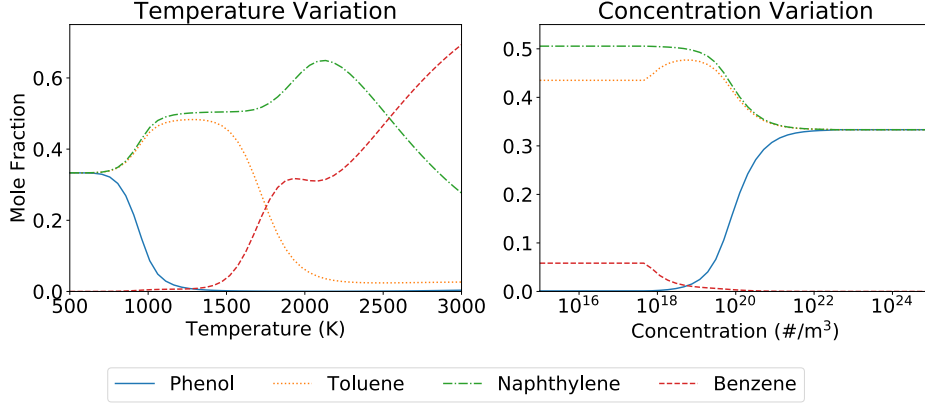


Figure 3.: Variations of time-averaged tar ratios from numerical study. On the left, temperature is varied while initial number density is kept constant. On the right, initial number density is varied while temperature is kept constant. In both, initial oxygen mass fraction, aromatic/aliphatic carbon ratio, and H₂ concentration are all kept constant.

where T is the temperature and C_l is the logarithm (base 10) of N_{tar} . Using the same methods discussed in Section 2.1, this model was calibrated yielding models for each x_i parameter,

$$x_{phe} = \frac{1}{6} \tanh(5.73 - 0.00384 T - 0.159 C_l) - 0.218 + 0.0277 C_l, \quad (13)$$

$$x_{naphth} = \frac{1}{2} \tanh(-1.98 + 6.18E-4 T + 0.124 C_l - 0.00285 C_l^2 + 4.14E-7 T^2 - 4.97E-5 T C_l) - 0.576 + 0.000233 T - 1.69E-7 T^2, \quad (14)$$

$$x_{tol} = \frac{1}{3} \tanh(17.3 - 0.00869 T - 1.08 C_l + 0.0199 C_l^2 + 0.000365 T C_l) + 0.000265 T - 0.000111 C_l^2 - 9.32E-6 T C_l, \quad (15)$$

$$x_{ben} = 1 - x_{phe} - x_{naphth} - x_{tol}, \quad (16)$$

which can be used to predict these type fractions with ease during model implementation. These empirical models produce decent results in comparison to the numerical study, as seen in Figure 4, which presents a parody plot where results of the numerical study are plotted against the x-axis while results of the surrogate model are plotted against the y-axis.

2.3. Soot Nucleation

Soot nucleation occurs through the coalescence of two tar molecules to form an incipient soot particle

$$r_{SN} = \epsilon \beta_T N_{tar}^2. \quad (17)$$

Here β_T represents a frequency of collision between tars and ϵ is a steric factor, the van der Waals enhancement factor, with a value of 2.2 [35]. This steric factor, was assumed to be constant in this work, consistent with past soot modeling work [6, 7, 36, 37]; however, more recent work on collision frequency provides an improvement to this factor [38]. From kinetic collision theory we can compute the frequency of collision between two molecules in the

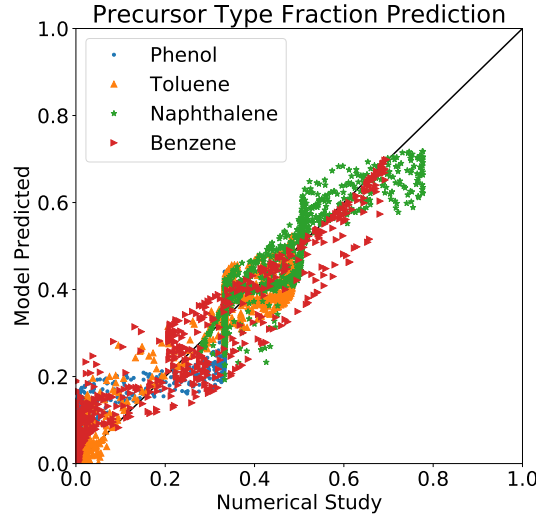


Figure 4.: Comparison between empirical model and numerical study for predicting tar-type fractions ($R^2=0.913$). The black straight 45° represents a perfect agreement between the two.

free-molecular regime

$$\beta_T = d_{tar}^2 \sqrt{\frac{8\pi k_B T}{m_{tar}}}, \quad (18)$$

where k_B is Boltzmann's constant, and d_{tar} , the effective diameter of the tar, can be computed using a geometric relationship [36]

$$d_{tar} = d_A \sqrt{\frac{2m_{tar}}{3m_C}}. \quad (19)$$

Note that Equation 17 represents the number of incipient soot particles created through the nucleation process. Two tar molecules are consumed for every one soot particle created; therefore, to obtain the total number of tar molecules consumed from soot nucleation multiply this term by 2 as seen in Equation 1.

2.4. Deposition

When a tar molecule collides with a soot particle, there is a likely chance that the tar will stick to the surface of the soot particle, thus growing the particle's surface. This is deposition process is modeled as,

$$r_{PD} = \varepsilon \beta_{TS} N_{tar} N_{soot}, \quad (20)$$

Table 3.: Surface growth mechanism where $k_i = AT^n \exp\left(\frac{-E}{RT}\right)$ [5].

No.	Reaction	A ($\frac{m^3}{kmol \cdot s \cdot K^n}$)	n	E ($\frac{J}{mole}$)
1	$C-H + H^\bullet \longrightarrow C^\bullet + H_2$	4.2×10^{10}		54,392
1R	$C-H + H^\bullet \longleftarrow C^\bullet + H_2$	3.9×10^9		46,024
2	$C-H + OH^\bullet \longrightarrow C^\bullet + H_2O$	1.0×10^7	0.734	5,932
2R	$C-H + OH^\bullet \longleftarrow C^\bullet + H_2O$	3.68×10^5	1.139	7,093
3	$C^\bullet + H^\bullet \longrightarrow C-H$	2.0×10^{10}		
4	$C^\bullet + C_2H_2 \longrightarrow C-H + H^\bullet$	8.0×10^4	1.56	15,762

using a frequency of collision, β_{TS} , between tar and soot particles. We compute the frequency of collision assuming a free-molecular collision regime

$$\beta_{TS} = (d_{soot} + d_{tar})^2 \sqrt{\frac{\pi k_B T}{2\mu_{TS}}}. \quad (21)$$

d_{tar} is the effective diameter of tar, computed using Equation 19, and d_{soot} is the effective diameter of the soot particles

$$d_{soot} = \left(\frac{6m_{soot}}{\pi\rho_s}\right)^{1/3}, \quad (22)$$

where m_{soot} is the mass of an individual soot particle defined as $m_{soot} = \frac{M_{soot}}{N_{soot}}$. μ_{TS} is the reduced mass of tar and soot

$$\mu_{TS} = \frac{m_{tar}m_{soot}}{m_{tar} + m_{soot}}. \quad (23)$$

These equations represent the rate of tar depositing on the surface of soot particles. To obtain the resulting mass accumulation, the second term in Equation 2, we simply multiple the number rate of tar deposition by the mass of the tar molecules being deposited.

2.5. Surface Reactions

We consider two types of surface reactions: surface growth, through the hydrogen-abstraction-carbon-addition mechanism (HACA), and consumption through oxidation and gasification.

HACA is an established growth mechanism [5, 39–41] which involves the attachment of acetylene molecules to a radicalized particle surface. Reactions of the mechanism are detailed in Table 3. Each reaction rate given in the table assumes a first order dependence on the gaseous species. The overall reaction rate (kg/m^2s) takes the form

$$R_{HACA} = 2m_C k_4 [C_2H_2] \alpha \chi_{C^\bullet}. \quad (24)$$

Table 4.: Parameters for surface consumption models found in Eqs. 30 and 31 [42].

Parameter	units	value	Equation
A_{O_2}	$\frac{kgK^{1/2}}{Pa\ m^2\ s}$	1.92E-3	30
E_{O_2}	$\frac{J}{mol}$	1.16E5	30
A_{OH}	$\frac{kgK^{1/2}}{Pa\ m^2\ s}$	2.93E-3	30
A_{CO_2}	$\frac{kg}{Pa^{1/2}K^2m^2s}$	1.92E-3	31
E_{CO_2}	$\frac{J}{mol}$	5.55E3	31
A_{H_2O}	$\frac{kgK^{1/2}}{Pa^0m^2s}$	1.92E-3	31
E_{H_2O}	$\frac{J}{mol}$	4.17E5	31

χ_{C^\bullet} represents a number density of sites on the particle surface which have been radicalized. The α parameter is the fraction of those surface sites kinetically available for reaction. Early implementations of HACA used an α value of 1 due to a lack of data. Appel et al. [5], derived an empirical correlation for calculating α ,

$$\alpha = \tanh\left(\frac{a}{\log \mu_1} + b\right), \quad (25)$$

where $\mu_1 = \frac{M_i}{N_i}$, and a and b are given as

$$a = 12.65 - 0.00563T, \quad (26)$$

$$b = -1.38 + 0.00068T. \quad (27)$$

The χ_{C^\bullet} value is computed using steady-state assumptions of the HACA mechanism in Table 3

$$\chi_{C^\bullet} = 2\chi_{C-H} \frac{k_1[H] + k_2[OH]}{k_{-1}[H_2] + k_{-2}[H_2O] + k_3[H] + k_4[C_2H_2]}. \quad (28)$$

χ_{C-H} is the number density of sites on the particle surface available for reaction, estimated to be 2.3×10^{19} sites/m² [5].

Use of Equation 25 requires the number and mass densities of a species. For soot this is not a problem as N_{soot} and M_{soot} are computed directly. For tars, number density is evaluated directly, N_{tar} , and mass density can be computed using the assumed molecular size,

$$M_{tar} = m_{tar}N_{tar}. \quad (29)$$

Oxidation and gasification rates are modeled as presented by Josephson et al. [42], given

as

$$R_{oxidation} = \frac{1}{T^{1/2}} \left(A_{O_2} P_{O_2} \exp \left[\frac{-E_{O_2}}{RT} \right] + A_{OH} P_{OH} \right), \quad (30)$$

$$R_{gasification} = A_{CO_2} P_{CO_2}^{0.5} T^2 \exp \left[\frac{-E_{CO_2}}{RT} \right] + A_{H_2O} P_{H_2O}^{1.21} T^{-1/2} \exp \left[\frac{-E_{H_2O}}{RT} \right], \quad (31)$$

which are functions of temperature (T), the ideal gas constant (R), and the partial pressures of O_2 , OH , CO_2 , and H_2O . Pre-exponential factors and activation energies given in Table 4.

The total effect of all four surface reactions, as a rate per unit of available surface area, is the sum of the individual processes

$$r_{SS} = r_{TS} = R_{HACA} - R_{oxidation} - R_{gasification}. \quad (32)$$

For tar, surface area is computed through an empirical correlation developed by Tielens [43] and results in the coefficient of the last term of Equation 1. This mass change of tar is then converted to an equivalent number of molecules produced or consumed assuming all molecules are a constant size. The surface area of soot is computed assuming spherical particles and the resulting area given in the last term of Equation 2.

2.6. Coagulation

Particle-particle coagulation only affects the number density term of soot particles since total soot mass is conserved throughout the process. The basic concept of coagulation is that two spherical particles collide, stick, and mold to form one larger particle that is still roughly spherical

$$r_{CS} = \beta_S N_{soot}^2. \quad (33)$$

Computing the frequency of collisions among soot particles is more difficult than among tars or between tars and particles. This is because soot particles can grow to very large sizes, large enough that soot particles can no longer be modeled with free-molecular collision regime assumptions, but rather as particles grow in size they increasingly show characteristics of a continuum collision regime. This model computes coagulation rates in both a free-molecular and continuum regime and uses the Knudsen number

$$Kn = \frac{2\lambda_p}{d_{soot}}, \quad (34)$$

a ratio of particle mean free path, λ_p , to particle diameter, to determine which regime we are in and which solution to use.

In the free-molecular regime, the frequency of particle collisions is computed in a way similar to those discussed before with the soot nucleation and tar deposition submodels,

$$\beta_S^f = \epsilon d_{soot}^2 \sqrt{\frac{8\pi k_B T}{m_{soot}}}, \quad (35)$$

where d_{soot} is computed from Equation 22.

In the continuum regime, the frequency of particle collision was modeled by Seinfeld and Pandis [44] as

$$\beta_S^c = \frac{8k_B T}{3\eta} (1 + 1.257Kn), \quad (36)$$

where η is the gas viscosity.

In the free-molecular regime, $Kn < 0.1$, we use β_S^f in Equation 33 to model the coagulation rate. In the continuum regime, $Kn > 10$, we use β_S^c in Equation 33. In the transition regime, $0.1 < Kn < 10$, we use a harmonic mean

$$\beta_S^t = \frac{\beta_S^c \beta_S^f}{\beta_S^c + \beta_S^f} \quad (37)$$

in Equation 33.

3. Simulations

This reduced soot model is proposed as an alternative to a previously developed detailed model [19] for systems that are too complex or computationally expensive for the detailed model. In this section, we compare the detailed and reduced models using two simulation configurations. The first is a flat flame burner configuration burning coal. The second is an LES using biomass.

3.1. Coal Flat-flame Burner

The first simulation involved a laminar flat-flame burner to which coal particles were injected. Details of this system were given by Ma et al. [46] and a schematic of the experimental set-up is shown in Figure 5. In the experiment, different coal types were injected into an established flame and a collection probe was set at different heights above the burner. In the collection probe, cool nitrogen quenched reacting gases and soot, char, and gases were separated and analyzed.

Experiments performed on the system were used previously to validate the developed detailed model with promising results. A series of validation simulations were carried out with details and results published previously [19]. One of these validation simulations was repeated in this work, using a Pittsburgh #8 coal and a flame temperature of 1650 K.

Figure 6 shows the results of these simulations where the proposed reduced model is directly compared against the previously-developed detailed model with great agreement between the two models. The left plot compares the predicted particle number density at different heights above the burner for the two models. The right plot compares the predicted soot volume fraction at those same heights. Here the reduced model initially tends to predict a slightly higher number density, which then shrinks at a rate faster than the detailed model eventually predicting a lower number density at long residence times. The initial higher particle number density is a result of the computed average of the reduced model. In contrast, the detailed model evaluates the tar distribution over 22 sections, 19 of which have mass higher than the computed average indicating that the vast number of particles are in those 3 sections smaller than the computed average. Smaller tar molecules tend to be consumed by thermal cracking faster than larger molecules. As a result, larger molecules, those in the higher sections, tend to make a higher percentage of soot particles in the detailed model, but in both

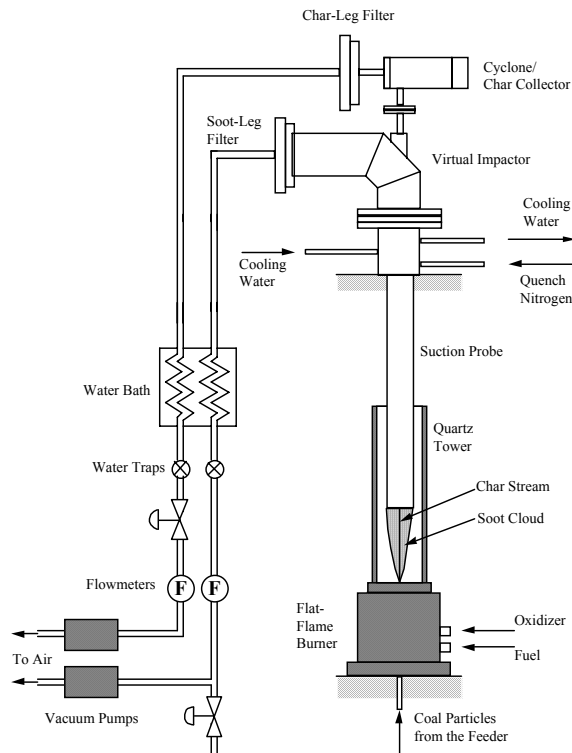


Figure 5.: Diagram of flat flame burner used by Ma [45]. Reproduced with permission.

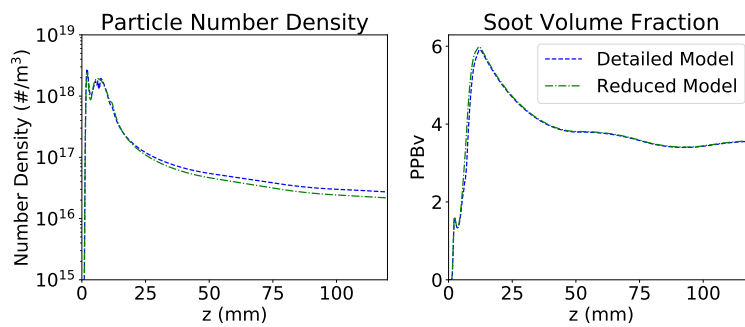


Figure 6.: Soot particle number density and volume fraction simulation results from the coal flat-flame burner, comparing reduced model against the detailed model.

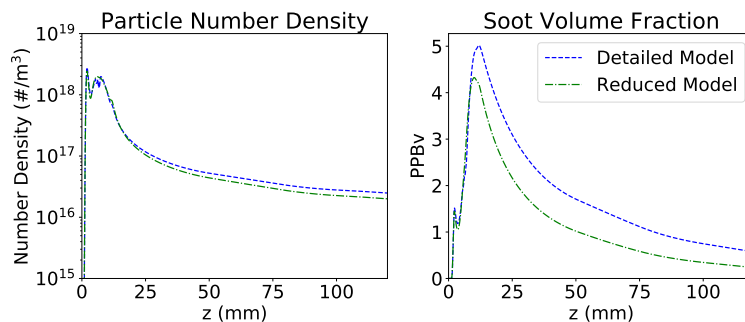


Figure 7.: Soot particle number density and volume fraction simulation results from the coal flat-flame burner with artificial oxidation throughout the reactor, comparing reduced model against the detailed model.

cases the total mass of tars going to soot is similar. Therefore, the total initial number of particles predicted by the reduced model is more than the detailed model.

After the initial formation of soot particles, coagulation becomes the dominant mechanism affecting particle number density. Rates of particle coagulation tend to be higher for the reduced model than for the detailed model. This is due to the mono-dispersed nature of the reduced model assumption. In the detailed model, small particles and large particles are colliding together at different frequencies dependent on the size of the particles. Inherently, there are a larger number of particles smaller than the average size than larger particles. This means that the majority of particles have a smaller particle diameter, which, along with particle speed, has a strong impact on the collision frequency of particles. Therefore, a slight decrease in collision frequency occurs in the detailed model compared to the reduced model which assumes all particles are the same average size. A higher collision frequency on the part of the reduced model leads to a higher rate of coagulation, as seen in the Figure.

In the experiment, coal particles are introduced into a fuel-rich flow and soot/char are collected by a suction probe before encountering an oxygen-rich region. Thus little to no soot oxidation occurs in the experimental set-up. In the model comparison here, an exploration of all mechanisms, including oxidation, is desirable, thus the simulation was executed again but with OH and O₂ kept constant, at 2 and 500 Pa respectively, throughout the simulation to compare the effects of oxidation on the soot profiles. Results of these oxidation simulations are shown in Figure 7.

The left image of Figure 7 compares the particle number density of the oxidation simulations and results do not vary noticeably from Figure 6. The right image, on the other hand, compares soot volume fraction predictions between the detailed and reduced models. Here there are significant differences between the detailed and reduced models. Oxidation reactions are more effective against particle distributions with higher surface area-to-volume ratios (SA/Vs) because the oxidation reactions attack the surface of particles. By averaging the mass and number densities for both tar and soot distributions in the reduced model, we have effectively lowered the SA/V ratio of the distributions because, although the bulk mass/volume of particles are larger, the bulk number of particles are smaller, and the average which maintains both the mass and number density shifts the overall SA/V ratio towards the smaller particles, thus oxidation becomes more effective.

This shift in SA/V is more severe in the tar distribution than in the soot distribution, and most of the differences seen in Figure 8 are attributed to this shift in the tar distribution. To demonstrate this, we performed another simulation where the OH and O₂ concentrations

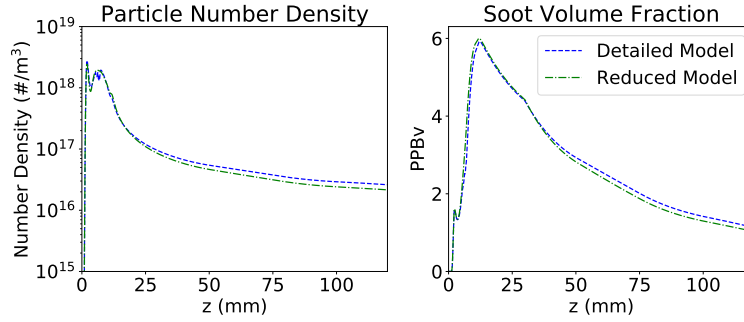


Figure 8.: Soot particle number density and volume fraction simulation results from the coal flat-flame burner with artificial oxidation imposed starting 30 mm into the reactor, comparing reduced model against the detailed model.

Table 5.: Computational expense comparison between the detailed model and this reduced model and found in the flat-flame burner simulation of Section 3.1.

	Detailed Model	Reduced Model
Final predicted particle number density ($\#/m^3$)	2.75E16	2.31E16
Final predicted soot volume fraction (<i>PPBV</i>)	2.62	2.27
Simulation time (s)	3298	4

were not adjusted until after the tar had either been converted to soot or thermally cracked, approximately 30 mm into the reactor, and results are shown in Figure 8. Here we see the ‘bend’ in results where the artificial oxidation takes effect at 30 mm. At this point there is an insignificant concentration of tar and so the oxidation is only affecting the established soot distribution. It is evident in this figure, that while predicted oxidation rate effects on the soot distribution are still higher for the reduced model than for the detailed model, the deviation is much smaller than it is for the tar distribution. This is consistent with the expected behavior of tar formation regions not coinciding with oxidatizing regions, whereas formed soot does encounter oxidizing zones.

The real advantage of this proposed reduced model lies in the reduced cost of execution. Table 5 quantitatively compares the final results of each simulation along with executional cost of each. As these simulations were relatively simple: one-dimensional and with chemistry and temperature profiles pre-established by experimentation, simulations could easily be executed on a single processor with code written in the Python language. The table shows that results of the two simulations gave very similar results, but the execution of the detailed model had 800 times the computational cost. Given the large difference in computational cost, and the difficulty and uncertainty in soot modeling, the agreement between the detailed and reduced models is exceptional.

3.2. LES Simulation

The coal flat-flame burner provided a good comparison between the two models but the system configuration is simple. To provide a more complex comparison of these two models with a real CFD approach, LES was performed of an oxy-fuel combustor (OFC) located at the University of Utah. These simulations were carried out to 7 seconds of simulation time

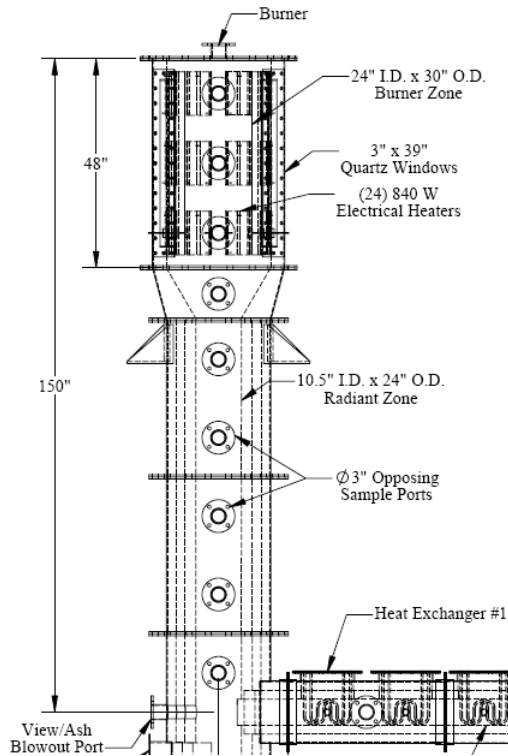


Figure 9.: Diagram of the downward burner and draft portion of the oxy-fuel combustor at the University of Utah.

using the LES software package Arches.

3.2.1. Oxy-Fuel Combustor

The OFC is a downward-fired 50 kilowatt lab-scale combustor unit [47]. Figure 9 shows a diagram of the combustion chamber and down-draft portion of the OFC; it does not show the full heat-exchanger portion which would extend to the right of the diagram. The burner of this unit contains a primary inlet and a secondary annulus inlet. Through the primary inlet fuel particles are fed with a carrier gas, while through the secondary inlet an oxidizer is fed. The oxidizer can be O_2 , an O_2/CO_2 mixture, or air, while the primary carrier gas is usually CO_2 or air. Walls of the reactor were heated to 1000 K.

The walls of the main combustion chamber are 0.6 m in diameter and 1.2 m long with heated walls so as to minimize boundary layer effects. Quartz windows are inlaid in the walls for visual observation and optical diagnostics in the main combustion chamber. Flue gases pass from the combustion zone to the radiation zone through a slight narrowing of the combustion chamber. All along the main combustion and radiation zones are a series of sample ports through which measurement instruments are installed. A purge gas, typically of CO_2 is blown over radiometers in these ports to protect the surfaces from the high heat flux and ash build-up. After the radiation zone, flue gases are sent through a series of heat exchangers before clean-up and ventilation.

Table 6.: Proximate and ultimate analysis for Douglas Fir biomass [29].

Moisture	Volatiles	Ash	C	H	N	S	O
1.50	81.50	0.80	52.30	6.30	0.10	0.01	40.50

Table 7.: Flow rates for the two simulated experiments.

Primary Inlet	
Fuel	5.22 (kg/hr)
CO ₂	4.29 (kg/hr)
O ₂	4.91 (kg/hr)
T	366.5 (K)
Secondary Inlet	
O ₂	30.25(kg/hr)
T	529.4 (K)
Over-fire Air	
O ₂	10.28(kg/hr)
T	529.4 (K)
Purge	
CO ₂	3.83 (kg/hr)
T	294.2 (K)

3.2.2. Arches Simulation

Both the detailed soot model and the reduced soot model of this work were implemented into Arches, which is built within the Uintah computational framework [48]. The reduced soot model could be implemented directly as presented in this work. However, the detailed model requires information about tar species, information discussed in Sections 2.1 and 2.2, including tar molecular sizes, yields, and chemistry mole fractions. To obtain these values, estimated reactor behavior (temperature, tar concentration, etc.) was fed into CPD and the numerical schemes and results discussed in those sections were coded into the simulation software rather than computed on-line.

Arches is a finite-volume LES-CFD software package under development at the University of Utah and was originally developed to simulate large pool-fires, by solving filtered Navier-Stokes equations at low Mach number using a pressure projection scheme and user-defined boundary conditions. Since its original development, Arches has been expanded with extensive particle physics to simulate solid-fuel flames. Now particulate fuels are traced in Arches simulations using an Eulerian particle transport method and the size-distribution of particles is represented using direct quadrature method of moments (DQMoM) with variable numbers of weights and abscissas. Variables describing the particles include the raw coal mass, three velocity components, char mass, particle weight, and enthalpy.

A variety of particle physics submodels are available in Arches. These include transport models for drag forces, thermophoresis, and thermal radiation, as well as source models for fuel swelling, devolatilization, char reactions, and ash-wall depositions. Chemistry profiles are tabulated by mixture fraction and enthalpy before simulation with an assumed equilibrium gas composition.

In these simulations, the fuel is a Douglas Fir biomass with Proximate and Ultimate anal-

yses shown in Table 6 and inlet conditions shown in Table 7. Douglas Fir is considered to be 46% Cellulose, 32% Hemicellulose, and 22% Lignin [49]. Fuel density is 650 kg/m³ and the raw fuel enthalpy is taken as -9.8477E5 J/kg. The fuel is represented by a particle distribution evaluated using direct quadrature method of moments with 3 quadrature nodes at initial sizes of 20, 120, and 240 μm particle diameters. Initially, the total weight of the fuel is divided up as 42.1% small particles, 30.6% medium particles, and 27.3% large particles. Internal coordinates of the fuel particle distribution include 3 coordinate velocities, temperature, number density, particle diameter, raw fuel mass, char mass, and particle enthalpy.

Fuel pyrolysis is modeled using a first-order weighted yield model (FOWY)

$$\frac{dV}{dt} = A_{devol} \exp\left(\frac{-E_{devol}}{R_{gas}T}\right) (V_{\infty} - V), \quad (38)$$

where V is the volatile yield of the parent fuel. This model was calibrated against CPDbio assuming a maximum temperature of 2300 K yielding values of 1.972E7 (1/s), 6.552E4 (J/mole), and 0.8596 for A_{devol} , E_{devol} , and V_{∞} , respectively. These parameters have a very small sensitivity to maximum temperatures above 1600 K as above that temperature biomass particles completely devolatilize well before approaching that temperature. At lower temperatures the parameter sensitivity quickly increases.

Char oxidation is modeled using a global reaction rate

$$\frac{dM_{char}}{dt} = A_{char} P_{O_2}^n \exp\left(\frac{-E_{char}}{R_{gas}T}\right), \quad (39)$$

where M_{char} is the consumption rate of carbon per m² of available surface area for oxidation. Values for A_{char} , E_{char} , and n were taken from work done by Murphy and Shaddix [50] and were 4.128 (kg/m² atm ^{n}), 45.5E6 (J/mol), and 0.18, respectively.

Thermal radiation was solved using discrete ordinates with 8 ordinates [51]. Absorption coefficients were computed for the grey gases and soot aerosol cloud using a correlation developed by Sarofim and Hottel [52, 53]. This model only accounts for absorption/emission properties of soot particles and grey gases based on experimental observations. It does not account for particle scattering and work is ongoing to improve capabilities in this CFD software.

Simulations were initiated with an empty reactor at atmospheric pressure and no initial radiated heat loss. A coal volatile mixture fraction of 0.065 and oxygen mixture fraction of 0.161, with the remaining mass being CO₂ are also initialized everywhere. No coal or soot particles are initialized in the domain.

3.2.3. Results

Under the above conditions, two simulations were carried out to provide a more complete comparison between the two proposed soot models. The first simulation used the detailed soot model with the tar distribution evaluated over 5 sections and the soot distribution evaluated over 6 moments. Proportions of the volatiles released as tar and partitioned into each evaluated section were computed pre-simulation by CPD using estimated particle temperature profiles. The second simulation used the reduced soot model with proportions of the volatiles released as tar along with the size of tar predicted by the sooting potential model of Section 2.1.

Figure 10 shows representative instantaneous soot profiles resulting from each simulation. Each image of the figure is a 2-dimensional cross-section of the combustion chamber 10 seconds into the simulation. Images (a) and (b) represent the soot volume fraction of each

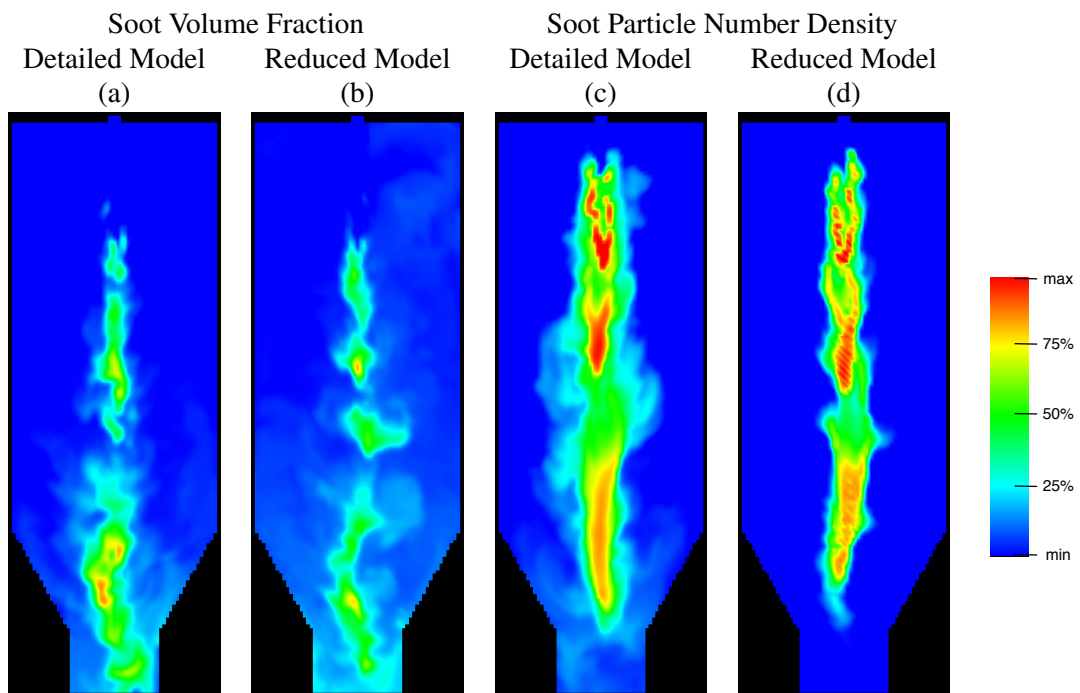


Figure 10.: Instantaneous results of the comparative LES coal simulations at 10 seconds of simulation time. From left to right the figures depict: (a) Soot volume fraction predicted by the detailed soot model, (b) by the reduced soot model (max = 5.0 ppmv, min = 0 ppmv), (c) soot particle number density on a log scale by the detailed model, (d) by the reduced model (max = $1E21$ $\#/m^3$, min = $1E16$ $\#/m^3$).

Table 8.: Computational expense comparison between the detailed model and the reduced model for the OFC simulation of Section 3.2.

	Detailed Model	Reduced Model
Lines of code to implement model in Arches	1233	613
Simulation CPU hours	11,292	3,684
Time-averaged centerline soot volume fraction (ppmv)	1.98	1.87

simulation while images (c) and (d) represent the particle number densities.

To better compare results from these simulations, we took obtained time-averaged soot volume fractions by averaging simulation outputs from 6.5 seconds to 7.5 seconds with outputs every 0.25 seconds. The first simulation, using the detailed model, predicts a time-averaged soot volume fraction of 1.31 ppmv along the reactor centerline, and the second simulation, using the reduced model predicts a soot volume fraction of 1.33 ppmv. While the reduced model predicts a slightly larger fraction of soot along the centerline, the detailed model predicts slightly larger quantities of soot across the entire reactor (approximately 3% more bulk soot volume fraction). As before, with the flat-flame burner, the number density of the detailed model simulation is smaller closer to the burner but with similar soot volume fraction, implying larger particles closer to the burner and therefore a smaller particle surface density, thus constraining consumption reactions more. Like the flat-flame burner simulations, the difference between these two models was small in the LES simulation and the overall trends are the same.

Another difference between the results of these two simulations comes from the rate of particle mixing. The detailed model captured slightly more dispersion of soot particles than the reduced model did, shown in the slightly lighter peripheries of the number density plots of images (a) and (c) of Figure 10. This slight increase in dispersion may be a result of a number of things, but most likely is an effect of diminished consumption rates in the detailed model simulations discussed above. These diminished consumption rates allowed particles to disperse more because a small amount of particles penetrated the flame’s reaction zone in the detailed model, but not in the reduced model.

In implementation, the detailed model evaluates a shape factor to reflect the morphology of particles. This shape factor is essentially a scale between $2/3$ and 1 where $2/3$ represents a minimum of surface area to volume ratio (a sphere) and 1 represents a maximum of that ratio. In the first simulation, the average shape factor of particles throughout the reactor was 0.69, and rarely exceeded 0.75. This indicates that a spherical representation of particles, an assumption made for the reduced model, was fairly accurate for this system.

While the two models predict small differences in the soot particle distribution across the reactor, the predictions are both comparable and promising to validate the proposed reduced model. The true advantages of the reduced model are shown in Table 8. Both of these simulations were executed with the same LES software, same resolution, same partitioning, and same operations. The only difference is the choice of soot model. This table shows that the complexity of model implementation, reflected in part by the number of lines of code, is much different. Implementing the reduced model is much simpler. At the same time, the computational cost, simulation CPU hours, is drastically reduced. While we recognize that the simulation CPU hours reported includes as aspects of the simulation (fluid dynamic computations, combustion reactions, radiative computations, etc.), the drastic reduction in the CPU hours when using the reduced model shows both the impact this simpler model may have on a large-scale simulation, and the large fraction of the overall simulation time required by the detailed model.

4. Conclusions

Computation of a fully detailed physics-based soot model comes at a high computational cost, and when implemented in large simulations becomes unreasonable. This work proposes a reduced model which significantly cuts computational costs by making two key assumptions: first that all particles are spherical and second that distributions in a simulation cell are mono-dispersed.

Along with the two stated assumptions, two surrogate models were also created. The first of these surrogate models, the sooting potential model, predicts the fraction of fuel volatiles which are tar and what the size of that tar is. Previously, soot modeling has depended on alternative means to predict tar outputs from primary pyrolysis, either using a detailed model, such as CPD, or using tabulated experimental data. The sooting potential here skirts these needs and directly predicts tar outputs. The second surrogate model is one for tar chemistry. The previously developed detailed model [19] required a numerical study to be performed for every simulation to predict fractions of surrogate type molecules which could represent tar. The new surrogate model bypasses the need for that numerical study and instead predicts type fractions in-situ.

The combination of the above mentioned assumptions, along with the application of the surrogate models, greatly reduces the mathematics and computational cost of soot formation modelling while maintaining a promising level of accuracy in predictive simulations.

The reduced soot model was applied in simulations of two different configurations and compared directly against identical simulations applying a more detailed model. The first simulation was of coal in a one-dimensional flat flame burner. Both the detailed and reduced models produced similar soot profiles with only small differences caused mostly by differences in particle coagulation rates. While profiles were very similar, the simulation time of the reduced model was much shorter (800 times) than that of the detailed model. The second simulation was of a biomass-fired oxy-fuel combustor. Predicted soot profiles were again very similar, but the reduced model was both easier to implement and the total computational cost was less, at approximately 1/3 the cost of the detailed model.

Given the significant economic advantage of the reduced model, we recommend its use in large-scale solid-fuel combustion simulations where effects of soot formation cannot be ignored but must be balanced with computational cost considerations.

Acknowledgements

We would like to extend deep gratitude to Dr. Thomas Fletcher and Dr. Jeremy Thornock who both reviewed the work in this article making some helpful suggestions and sharing their insight.

In addition, we gratefully acknowledge the Los Alamos National Laboratory's Institutional Computing Program and Brigham Young University's Office of Research Computing for providing computational resources.

Funding

This work was supported by the Department of Energy, National Nuclear Security Administration under Award DE-NA0002375, and by the United States Department of Agriculture Forest Service through the Rocky Mountain Research Station to develop an understanding of emissions formation in wildfires.

Nomenclature

Variable	Meaning	Units
A_i	Pre-exponential constant for process i	Varies
C_l	Log of species concentration	$\log\left(\frac{\#}{m^3}\right)$
d_i	Collision diameter of species i	m
E_i	Activation energy for process i	$\frac{J}{mole}$
k_B	Boltzmann constant (1.38064852e-23)	$\frac{m^2 kg}{s^2 K}$
k_i	Kinetic rate constant	$\frac{m^3}{kmol s}$
Kn	Knudsen number	—
H_C	Atomic ratio of hydrogen to carbon	—
m_i	Molecular mass of species i	kg
N_i	Particles/molecules of species i	$\frac{\#}{m^3}$
O_C	Atomic ratio of oxygen to carbon	—
P_i	Partial pressure of species i	Pa
P_l	Log of pressure (base 10)	$\log(Pa)$
r_i	Rate of change of process i	$\frac{\#}{m^3 s}$ or $\frac{kg}{m^3 s}$
R	Ideal gas constant	$\frac{J}{mole \cdot K}$
R_i	Rate of process i	$\frac{kg}{m^2 s}$
t	Time	s
$T(g)$	Local temperature of gas	K
V	Volatile matter content	—
x_i	Mole fraction of species i	—
y_i	Mass fraction of species i	—
β_{ij}	Frequency of collision between species i and j or i with itself	$\frac{m^3}{s}$
ϵ	Van der Waals enhancement factor	—
η	Gas viscosity	$\frac{kg}{m s}$
λ_p	Particle mean free path	m
ρ_s	Soot density	$\frac{kg}{m^3}$
$[i]$	Concentration of species i	$\frac{kmole}{m^3}$

References

- [1] Z.A. Mansurov, *Soot formation in combustion processes (review)*, Combustion, Explosion and Shock Waves 41 (2005), pp. 727–744.
- [2] S. Salenbauch, A. Cuoci, A. Frassoldati, C. Saggese, T. Faravelli, and C. Hasse, *Modeling soot formation in premixed flames using an Extended Conditional Quadrature Method of Moments*, Combustion and Flame 162 (2015), pp. 2529–2543.
- [3] H. Bockhorn, *Soot formation in combustion: mechanisms and models*, Springer-Verlag, Berlin ; New York, 1994.
- [4] I.M. Kennedy, *Models of soot formation and oxidation*, Progress in Energy and Combustion Science 23 (1997), pp. 95–132.

- [5] J. Appel, H. Bockhorn, and M. Frenklach, *Kinetic Modeling of Soot Formation with Detailed Chemistry and Physics: Laminar Premixed Flames of C₂ Hydrocarbons*, *Combustion and Flame* 121 (2000), pp. 122–136.
- [6] M. Frenklach, *Method of moments with interpolative closure*, *Chemical Engineering Science* 57 (2002), pp. 2229–2239.
- [7] M.E. Mueller, G. Blanquart, and H. Pitsch, *A joint volume-surface model of soot aggregation with the method of moments*, *Proceedings of the Combustion Institute* 32 (2009), pp. 785–792.
- [8] S. Hong, M.S. Wooldridge, H.G. Im, D.N. Assanis, and H. Pitsch, *Development and application of a comprehensive soot model for 3D CFD reacting flow studies in a diesel engine*, *Combustion and Flame* 143 (2005), pp. 11–26.
- [9] M. Sirignano, J.H. Kent, and A. D’Anna, *Modeling Formation and Oxidation of Soot in Non-premixed Flames*, *Energy & Fuels* 27 (2013), pp. 2303–2315.
- [10] A.L. Brown and T.H. Fletcher, *Modeling Soot Derived from Pulverized Coal*, *Energy & Fuels* 12 (1998), pp. 745–757.
- [11] M. Muto, K. Yuasa, and R. Kurose, *Numerical simulation of soot formation in pulverized coal combustion with detailed chemical reaction mechanism*, *Advanced Powder Technology* 29 (2018), pp. 1119–1127.
- [12] H.F. Calcote, *Mechanisms of Soot Nucleation in Flames - a Critical-Review*, *Combustion and Flame* 42 (1981), pp. 215–242.
- [13] H. Wang, *Formation of nascent soot and other condensed-phase materials in flames*, *Proceedings of the Combustion Institute* 33 (2011), pp. 41–67.
- [14] T.H. Fletcher, J. Ma, J.R. Rigby, A.L. Brown, and B.W. Webb, *Soot in coal combustion systems*, *Progress in Energy and Combustion Science* 23 (1997), pp. 283–301.
- [15] E.M. Fitzpatrick, K.D. Bartle, M.L. Kubacki, J.M. Jones, M. Pourkashanian, A.B. Ross, A. Williams, and K. Kubica, *The mechanism of the formation of soot and other pollutants during the co-firing of coal and pine wood in a fixed bed combustor*, *Fuel* 88 (2009), pp. 2409–2417.
- [16] J.R. Rigby, J. Ma, B.W. Webb, and T.H. Fletcher, *Transformations of Coal-Derived Soot at Elevated Temperature*, *Energy and Fuels* 15 (2001), pp. 52–59.
- [17] J. Trawczynski, *Catalytic combustion of soot*, *Reaction Kinetics and Catalysis Letters* 63 (1998), pp. 41–45.
- [18] M.S. Safdari, M. Rahmati, E. Amini, J.E. Howarth, J.P. Berryhill, M. Diertenberger, D.R. Weise, and T.H. Fletcher, *Characterization of pyrolysis products from fast pyrolysis of live and dead vegetation native to the Southern United States*, *Fuel* 229 (2018), pp. 151–166.
- [19] A.J. Josephson, R.R. Linn, and D.O. Lignell, *Modeling soot formation from solid complex fuels*, *Combustion and Flame* 196 (2018), pp. 265–283.
- [20] H. Watanabe, R. Kurose, S. Komori, and H. Pitsch, *Effects of radiation on spray flame characteristics and soot formation*, *Combustion and Flame* 152 (2008), pp. 2–13.
- [21] P.R. Lindstedt, *Simplified soot nucleation and surface growth steps for non-premixed flames*, in *Soot formation in combustion: mechanisms and models*, 59, Springer-Verlag, New York, 1994, pp. 417–441.
- [22] C.W. Lautenberger, J.L. de Ris, N.A. Dembsey, J.R. Barnett, and H.R. Baum, *A simplified model for soot formation and oxidation in CFD simulation of non-premixed hydrocarbon flames*, *Fire Safety Journal* 40 (2005), pp. 141–176.
- [23] K. Yamamoto, T. Murota, T. Okazaki, and M. Taniguchi, *Large eddy simulation of a pulverized coal jet flame ignited by a preheated gas flow*, *Proceedings of the Combustion Institute* 33 (2011), pp. 1771–1778.
- [24] A.P. Richards and T.H. Fletcher, *A comparison of simple global kinetic models for coal devolatilization with the CPD model*, *Fuel* 185 (2016), pp. 171–180.
- [25] H. Kobayashi, J.B. Howard, and A.F. Sarofim, *Coal devolatilization at high temperatures*, *Symposium (International) on Combustion* 16 (1977), pp. 411–425.
- [26] T.H. Fletcher, A.R. Kerstein, R.J. Pugmire, M.S. Solum, and D.M. Grant, *Chemical percolation model for devolatilization. 3. Direct use of carbon-13 NMR data to predict effects of coal type*, *Energy & Fuels* 6 (1992), pp. 414–431.
- [27] A.D. Lewis and T.H. Fletcher, *Prediction of Sawdust Pyrolysis Yields from a Flat-Flame Burner*

- Using the CPD Model*, Energy & Fuels 27 (2013), pp. 942–953.
- [28] D. Genetti, T.H. Fletcher, and R.J. Pugmire, *Development and Application of a Correlation of ¹³C NMR Chemical Structural Analyses of Coal Based on Elemental Composition and Volatile Matter Content*, Energy & Fuels 13 (1999), pp. 60–68.
- [29] C.J. Biermann, *Handbook of Pulping and Papermaking*, Academic Press, 1996.
- [30] K.R. Doolan, J.C. Mackie, and R.J. Tyler, *Coal flash pyrolysis: secondary cracking of tar vapours in the range 870-2000 K*, Fuel 66 (1987), pp. 572–578.
- [31] M.A. Serio, W.A. Peters, and J.B. Howard, *Kinetics of vapor-phase secondary reactions of prompt coal pyrolysis tars*, Industrial & Engineering Chemistry Research 26 (1987), pp. 1831–1838.
- [32] F. Dabai, N. Paterson, M. Millan, P.S. Fennell, and R. Kandiyoti, *Tar Formation and Destruction in a Fixed Bed Reactor Simulating Downdraft Gasification: Effect of Reaction Conditions on Tar Cracking Products*, Energy & Fuels 28 (2014), pp. 1970–1982.
- [33] Y.B. Mao, Y.P. Dong, B. Wang, J.F. Chang, J. Yu, Y. Zhang, Y. Huo, and C.S. Sun, *Characteristics and kinetics of biomass tar cracking in a micro fluidized bed*, RSC Advances 5 (2015), pp. 82845–82852.
- [34] F. Marias, R. Demarthon, A. Bloas, and J.P. Robert-arnouil, *Modeling of tar thermal cracking in a plasma reactor*, Fuel Processing Technology 149 (2016), pp. 139–152.
- [35] M. Frenklach and S.J. Harris, *Aerosol dynamics modeling using the method of moments*, Journal of Colloid And Interface Science 118 (1987), pp. 252–261.
- [36] M. Frenklach and H. Wang, *Detailed Mechanism and Modeling of Soot Particle Formation*, in *Soot Formation in Combustion*, Springer-Verlag, 1994, pp. 165–192.
- [37] P.R. Lindstedt and S.A. Louloudi, *Joint-scalar transported PDF modeling of soot formation and oxidation*, Proceedings of the Combustion Institute 30 (2005), pp. 775–782.
- [38] H. Ouyang, R. Gopalakrishnan, and C.J. Hogan, *Nanoparticle collisions in the gas phase in the presence of singular contact potentials*, Journal of Chemical Physics 137 (2012).
- [39] M. Frenklach and H. Wang, *Detailed modelling of soot particle nucleation and growth*, Symposium (International) on Combustion 23 (1990), pp. 1559–1566.
- [40] R.S. Mehta, D.C. Haworth, and M.F. Modest, *An assessment of gas-phase reaction mechanisms and soot models for laminar atmospheric-pressure ethylene-air flames*, Proceedings of the Combustion Institute 32 I (2009), pp. 1327–1334.
- [41] T.J. McKinnon and J.B. Howard, *The roles of pah and acetylene in soot nucleation and growth*, Symposium (International) on Combustion 24 (1992), pp. 965–971.
- [42] A.J. Josephson, N.D. Gaffin, S.T. Smith, T.H. Fletcher, and D.O. Lignell, *Modeling Soot Oxidation and Gasification with Bayesian Statistics*, Energy and Fuels 31 (2017), pp. 11291–11303.
- [43] A.G.G.M. Tielens, *The Physics and Chemistry of the Interstellar Medium*, Cambridge University Press, Cambridge, 2005.
- [44] J.H. Seinfeld and S.N. Pandis, *Atmospheric Chemistry and Physics: From Air Pollution to Climate Change.*, Vol. 2, John Wiley, New York, 2006.
- [45] J. Ma, *Soot Formation During Coal Pyrolysis*, Thesis, Brigham Young University, 1996.
- [46] J. Ma, T.H. Fletcher, and B.W. Webb, *Conversion of coal tar to soot during coal pyrolysis in a post-flame environment*, Symposium (International) on Combustion 26 (1996), pp. 3161–3167.
- [47] C.K. Stimpson, A. Fry, T. Blanc, and D.R. Tree, *Line of sight soot volume fraction measurements in air- and oxy-coal flames*, Proceedings of the Combustion Institute 34 (2013), pp. 2885–2893.
- [48] S.G. Parker, *A component-based architecture for parallel multi-physics PDE simulation*, Future Generation Computer Systems 22 (2006), pp. 204–216.
- [49] V. Pasangulapati, K.D. Ramachandriya, A. Kumar, M.R. Wilkins, C.L. Jones, and R.L. Huhnke, *Effects of cellulose, hemicellulose and lignin on thermochemical conversion characteristics of the selected biomass*, Bioresource Technology 114 (2012), pp. 663–669.
- [50] J.J. Murphy and C.R. Shaddix, *Combustion kinetics of coal chars in oxygen-enriched environments*, Combustion and Flame 144 (2006), pp. 710–729.
- [51] M.F. Modest, *Radiative Heat Transfer*, 3rd ed., Academic Press, 2013.
- [52] A.F. Sarofim and H.C. Hottel, *Radiative transfer in combustion chambers: influence of alternative fuels*, in *Sixth International Heat Transfer Conference*, Washington, DC, USA. National Research

- Council Canada, Hemisphere Publishing Corp., 1978, pp. 199–217.
- [53] H.C. Hottel, A.F. Sarofim, L.B. Evans, and I.A. Vasalos, *Radiative Transfer in Anisotropically Scattering Media: Allowance for Fresnel Reflection at the Boundaries*, *Journal of Heat Transfer* 90 (1968), pp. 56–62.